Opto-Electronic Advances

Supplementary information

April 2023, Vol. 6, No. 4

DOI: 10.29026/oea.2023.220133

Tailoring spatiotemporal dynamics of plasmonic vortices

Xinyao Yuan[1], Quan Xu[1]*, Yuanhao Lang[1], Xiaohan Jiang[1], Yuehong Xu[1], Xieyu Chen[1], Jie Han[1], Xueqian Zhang[1], Jiaguang Han[1,2]* and Weili Zhang[3]*

[1]Center for Terahertz Waves and College of Precision Instrument and Optoelectronics Engineering, Tianjin University and the Key Laboratory of Optoelectronics Information and Technology (Ministry of Education), Tianjin 300072, China; [2]Guangxi Key Laboratory of Optoelectronic Information Processing, School of Optoelectronic Engineering, Guilin University of Electronic Technology, Guilin 541004, China; [3]School of Electronic and Computer Engineering, Oklahoma State University, Stillwater, OK 74078, USA.

*Correspondence: Q Xu, E-mail: quanxu@tju.edu.cn; JG Han, E-mail: jiaghan@tju.edu.cn; WL Zhang, E-mail: weili.zhang@okstate.edu

This file includes:

Supplementary information for this paper is available at https://doi.org/10.29026/oea.2023.220133

Section 1: Topological charge of plasmonic vortex generated by our proposed couplers.

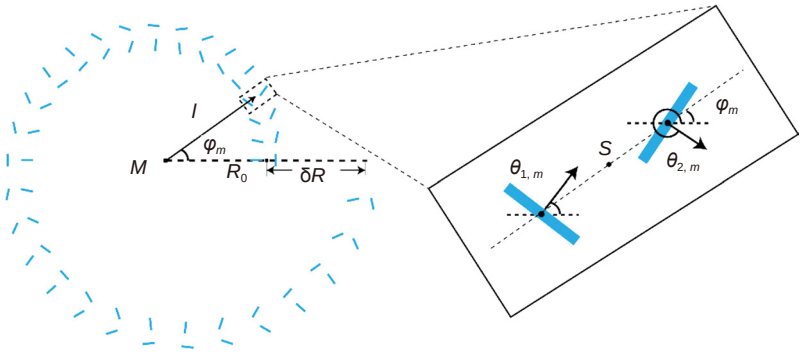

Fig. S1 | Top views of the plasmonic vortex coupler composed by *m* slit-pairs arranged in an Archimedean spiral-shape and zoomed-in view of a single slit-pair.

Considering a slit pair, as illustrated in Fig. S1, is excited at normal incidence by a plane wave with electric field $\boldsymbol{E}_{\rm in}$, the field at the center point M is the superposition of the surface wave fields from the two slit apertures:

$$\boldsymbol{E}_M = \frac{\eta\hat{a}}{\mathrm{i}\sqrt{\lambda_{\rm SP}}}\left[\frac{(\boldsymbol{E}_{\rm in}\cdot\hat{n}_1)\,\mathrm{e}^{\mathrm{i}k_{\rm SP}|l-S/2|}\cos\left(\theta_1-(\pi+\varphi_m)\right)}{\sqrt{|l+S/2|}}+\frac{(\boldsymbol{E}_{\rm in}\cdot\hat{n}_2)\,\mathrm{e}^{\mathrm{i}k_{\rm SP}|l+S/2|}\cos\left(\theta_2-(\pi+\varphi_m)\right)}{\sqrt{|l-S/2|}}\right]. \tag{S1}$$

Here, E_M is the complex amplitude of the SP field at point M; η is the conversion efficiency from incident light to SPs; $k_{\rm SP}=2\pi/\lambda_{\rm SP}$ is the SP wave number; $\hat{a}$ is the unit vector from the center of mth slit pair to the point M. Since the two slits are designed with distance $S=\lambda_{\rm SP}/2$, it can be concluded that:

$$\begin{aligned}\mathrm{e}^{\mathrm{i}k_{\rm SP}|l+S/2|} &= i\,\mathrm{sign}(l)\mathrm{e}^{\mathrm{i}k_{\rm SP}|l|},\\ \mathrm{e}^{\mathrm{i}k_{\rm SP}|l-S/2|} &= -i\,\mathrm{sign}(l)\mathrm{e}^{\mathrm{i}k_{\rm SP}|l|}.\end{aligned} \tag{S2}$$

Considering $|l|\gg S/2$, we can approximate $1\Big/\sqrt{l\pm S/2}\approx 1/\sqrt{|l|}$. And Eq. (S1) can be expressed as:

$$\boldsymbol{E}_M = \frac{\eta\hat{a}}{\sqrt{\lambda_{\rm SP}\,|l|}}\mathrm{sign}\,(l)\,\mathrm{e}^{\mathrm{i}k_{\rm SP}|l|}\left[(\boldsymbol{E}_{\rm in}\cdot\hat{\boldsymbol{n}}_2)\cos\left(\theta_2-(\pi+\varphi_m)\right)-\mathrm{i}\,(\boldsymbol{E}_{\rm in}\cdot\hat{\boldsymbol{n}}_1)\cos\left(\theta_1-(\pi+\varphi_m)\right)\right]. \tag{S3}$$

Under the CP normal incidence $\boldsymbol{E}_{\rm in}=\begin{pmatrix}\sqrt{2}/2 & \sigma i\sqrt{2}/2\end{pmatrix}$, the SP field at point M can be calculated as:

$$\begin{aligned}\boldsymbol{E}_M &= \frac{\sqrt{2}}{2}\frac{\eta\hat{a}}{\sqrt{\lambda_{\rm SP}\,|l|}}\mathrm{sign}\,(l)\,\mathrm{e}^{\mathrm{i}k_{\rm SP}|l|}\left[(\cos\theta_2+\sigma\mathrm{i}\sin\theta_2)\cos\left(\theta_2-(\pi+\varphi_m)\right)-(\cos\theta_1+\sigma\mathrm{i}\sin\theta_1)\cos\left(\theta_1-(\pi+\varphi_m)\right)\right]\\ &= \frac{\sqrt{2}}{2}\frac{\eta\hat{a}}{\sqrt{\lambda_{\rm SP}\,|l|}}\mathrm{sign}\,(l)\,\mathrm{e}^{\mathrm{i}k_{\rm SP}|l|}\mathrm{e}^{\mathrm{i}\sigma\left(\theta_2+\theta_1-(\pi+\varphi_m)+\pi/2\right)}\sin\left(\theta_2-\theta_1\right).\end{aligned} \tag{S4}$$

With the definition of $\theta_{1,m}$, $\theta_{2,m}$ and R_m in Eqs. (3) and (4) of the manuscript, Eq. (S4) can be simplified to:

$$\begin{aligned}\boldsymbol{E}_M &= \frac{\sqrt{2}}{2}\frac{\eta\hat{a}}{\sqrt{\lambda_{\rm SP}\,|l|}}\mathrm{e}^{\mathrm{i}(k_{\rm SP}R_0+2\sigma\alpha_0)}\mathrm{e}^{\mathrm{i}p\varphi_m}\mathrm{e}^{\mathrm{i}\sigma\left(g\varphi_m-\varphi_m\right)}\\ &= \frac{\sqrt{2}}{2}\frac{\eta\hat{a}}{\sqrt{\lambda_{\rm SP}\,|l|}}\mathrm{e}^{\mathrm{i}(k_{\rm SP}R_0+2\sigma\alpha_0)}\mathrm{e}^{\mathrm{i}(\sigma(g-1)+p)\varphi_m}.\end{aligned} \tag{S5}$$

So the topological charge of generated plasmonic vortex can be expressed as:

$$l=\sigma(g-1)+p. \tag{S6}$$

Section 2: Waveform deviation caused by dispersion.

In theory, the waveform variation due to dispersion should be taken into consideration when we generalize the 2D Huygens-Fresnel principle to the time domain. In the visible and infrared regimes, the wave vectors of surface waves $k_{\rm SP}$ are obviously larger than that of light in vacuum k_0, so the dispersion is more obvious. While in the terahertz regime, $k_{\rm SP}$ is

similar to k_0, so the attenuation of the surface wave field along the z direction is very small. Therefore, the SPs cannot be confined as well at the metal surfaces as in the visible regime. To increase the confinement, all the samples are covered with a 10 μm thick polyimide layer. Now, we investigate the influence of dispersion on the radiation waveforms.

The eigen-mode solver of *CST Microwave Studio* was employed to calculate the corresponding dispersion relation for the fundamental mode at the first Brillouin zone. The basic unit was set to be a PEC square with side length a = 100 μm covered by a 10-μm-thick lossless dielectric layer (polyimide, $\varepsilon_{\text{polyimide}}$ =2.96). Periodic boundaries were applied in both the x and y directions. There was a vacuum box of 1000 μm height above the unit. The calculated dispersion relation is shown in Fig. S2(a). It can be concluded that there is a very small difference between these two lines and the difference increases slowly as the frequency increases. Figure S2(b) illustrates the detailed dispersion relations at the interested frequency, marked by a dotted line in Fig. S2(a). In this case, the $k_{\text{SP}} \approx 1.0094k_0$ at 0.75 THz.

With this relation, we can calculate the waveform deviation caused by dispersion after SP propagating arbitrary distance from the slit resonator. Since the plasmonic vortex couplers are designed with R_0 = 1000 μm and the area we care about is relatively small, here we compare the SP waveforms propagating d = 2000 μm in the vacuum and in the polyimide layer for example. The result is shown in Fig. S2(c). The two curves are basically consistent without significant difference on the whole and the SP waveform in the polyimide layer is slightly behind that in vacuum due to the lower propagation speed. Since the waveform variation caused by dispersion is relatively small, we can neglect this in our numerical calculation to simplify operations, and the time-domain 2D Huygens-Fresnel principle can also be applied to the infrared and visible regimes.

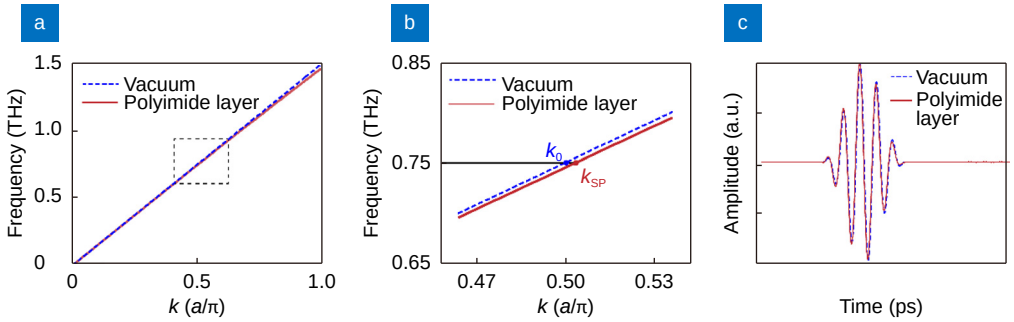

Fig. S2 | (**a**) Dispersion relation of the metal surface covered by a polyimide layer, here a = 100 μm. (**b**) Zoomed-in view of the central part of (a). (**c**) The SP waveforms propagating d = 2000 μm after excited from the slit resonator.

Section 3: OAM spectrum of the generated plasmonic vortices.

We extracted the complex SP fields $E(\theta)$ of the two couplers along the target orbit of fourth-order plasmonic vortex, the radius of which is about 340 μm. As different OAM components (with different topological charges) are perpendicular to each other and thus can be seen as a group of orthogonal bases, we expand $E(\theta)$ using this basis to obtain the strength of each OAM component. By performing the Fourier transform of $E(\theta)$ on the azimuthal angle θ, one can get the corresponding topological charge spectrum of each OAM component.

The results are shown in Fig. S3(a) and S3(b), respectively for Sample 1 and Sample 2. The target OAM component of fourth-order is the strongest in both numerical and experimental results, whereas the other OAM components are quite weak, which comply well with expectation, confirming the accuracy of our proposed temporal OAM manipulation method.

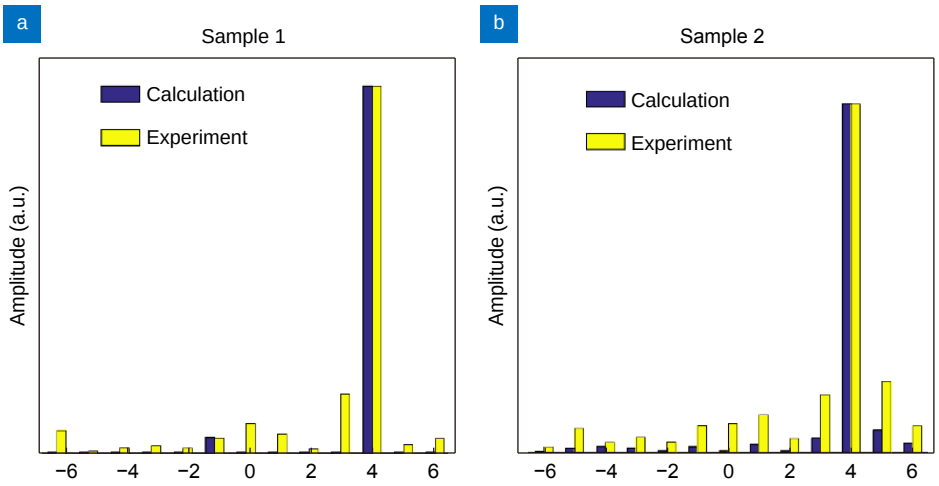

Fig. S3 | (**a**) and (**b**) illustrate the OAM spectrum extracted from the numerical (blue) and experimental (yellow) results along the target orbit of fourth-order plasmonic vortex for Sample 1 and Sample 2, respectively.

Section 4: The difference between numerically generated SP waveform and the simulated SP waveform generated from an actual slit resonator.

In numerical calculation, the radiation waveform is generated by the following function:

$$E(t) = A \cdot (H(t) - H(t - N/f_c)) \cdot (1 - \cos(2\pi f_c t/N)) \cdot \sin 2\pi f_c t\ , \tag{S7}$$

where $H(t)$ represents the Heaviside step function. A is the amplitude value of the generated signal. N represents the number of peaks in the signal. f_c is the center frequency. And the time series is set by $t = 0$: dt: T, with $T = nT_0$. Here, T is the total duration of the waveform signal and T_0 is the oscillation time. With this function, one can generate desired waveform to simulate the resonant response of different slit resonators through setting corresponding parameters, such as the f_c, N and so on. The simulation waveform employed in the manuscript is generated by choosing $A = 1$, $N = 5$, $f_c = 0.75$ THz, $T_0 = 8$ ps, $n = 5$ and $T = 40$ ps.

In experiments, since the sample is designed to be 70 slit-pairs, we cannot directly obtain the response of a single slit resonator to the incident light. *CST Microwave Studio* was employed to simulate the corresponding waveform. We experimentally measured the time-domain signal of the incident light, that is, the terahertz radiation after collimated by the lens in Fig. 4 of the manuscript, and use it as reference for the excitation signal instead of the default signal in the software. A sandwiched structure consisting of a 10 μm-thick photoresist upper layer, a 0.2 μm-thick Aluminum middle layer, and a silicon bottom layer was considered in the simulation. The upper surface of the silicon substrate was set to be the plane of $z = 0$, and all the layers were square with 2000 μm side length. The slit aperture parallel to the y-axis was set at the origin with dimension of 70 μm × 10 μm, identical with the sample design. In this case, RCP was used to excite the structures from the substrate side and SPs at wavelength $\lambda_{SP} = 400$ μm were coupled on the metal surface. The

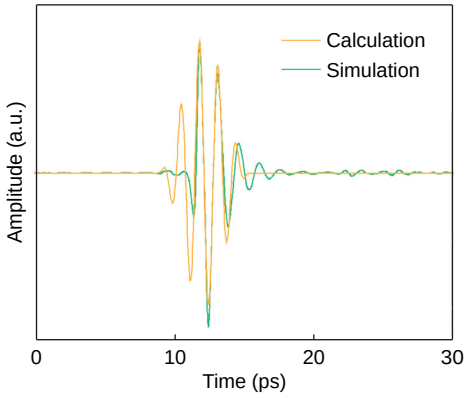

Fig. S4 | Diagrams of the numerically generated SP waveform (orange) and the simulated result of SP waveform generated from an actual slit resonator (green).

probe was placed at the point (1000, 0, 50) to record E_z component of the electromagnetic field during the transient analysis to acquire the radiation waveform. The results are shown in Fig. S4. The two curves basically match on the trend but with some differences in amplitude, which lead to the deviations between numerical and actual experimental results.

Section 5: Videos of generated plasmonic vortices' detailed evolution processes.

The results in Fig. 5(g) and 5(i) are evolution snapshots with an interval of 1 ps, while the waveforms $\mathbf{S}_{x,y}^{\pm 45^\circ}(t)$ were obtained with consecutive time steps of 20 fs in our experiments, so it is possible to reveal the evolution processes in deeper sub-optical-cycle tempol resolution. Please find the enclosed videos entitled "Supplemental Videos S1" and "Supplemental Videos S2" to get the detailed information.

Section 6: Additional three plasmonic vortex couplers and their corresponding experimental results.

We fabricated additional three coupler samples and conducted the same experiments using the fiber-based NSTM system. Figure S5 show the microscopic photos of fabricated samples. All the measurements were obtained at the plane that about 75 μm above the sample surface under the RCP incidence, and the scanned range was set to be 2 mm × 2 mm, identical with these two samples in the manuscript. The frequency-domain results are shown in Fig. S6 and the spatiotemporal dynamics are shown in Fig. S7.

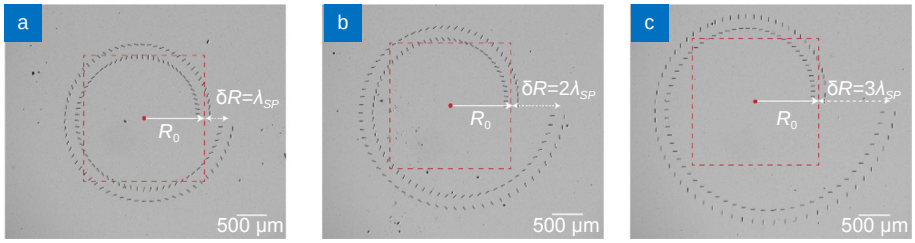

Fig. S5 | Microscope images of designed another three plasmonic vortex coupler samples by introducing different propagation phase. They consist of 70 pairs of slit resonators which are arranged in the Archimedean spiral configuration with R_0 = 1000 μm, $\delta R = p\lambda_{SP}$, and p = 1, 2, 3, corresponding to (**a**), (**b**) and (**c**), respectively. The red dotted boxes represent the area we care about in experiments, a square with sides of 2000 μm.

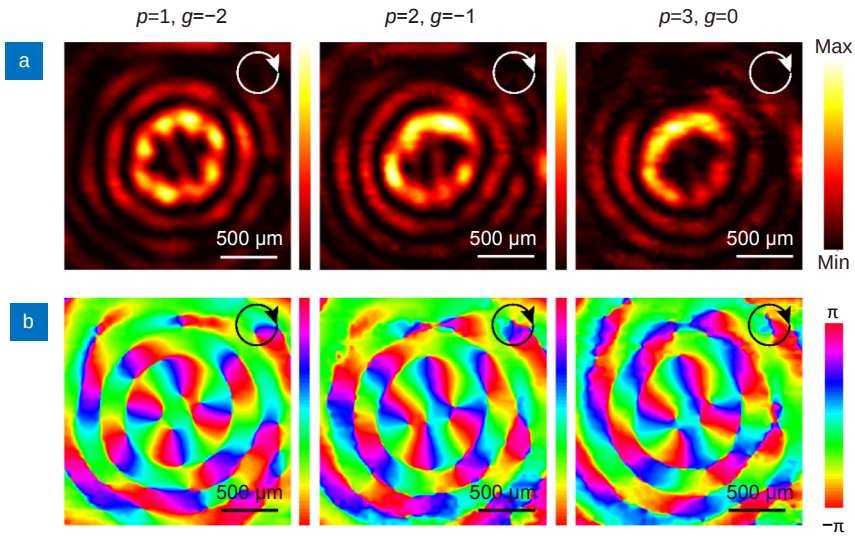

Fig. S6 | Experimental results of the additional three plasmonic vortex couplers in frequency-domain. (**a**) The measured intensity distributions of the SPs field under the RCP incidence, corresponding to p = 1, 2, 3 in turn. (**b**) Corresponding phase distributions of the three samples. The inset circles at the top-right corner denote the spin direction of corresponding incidence, similar hereinafter.

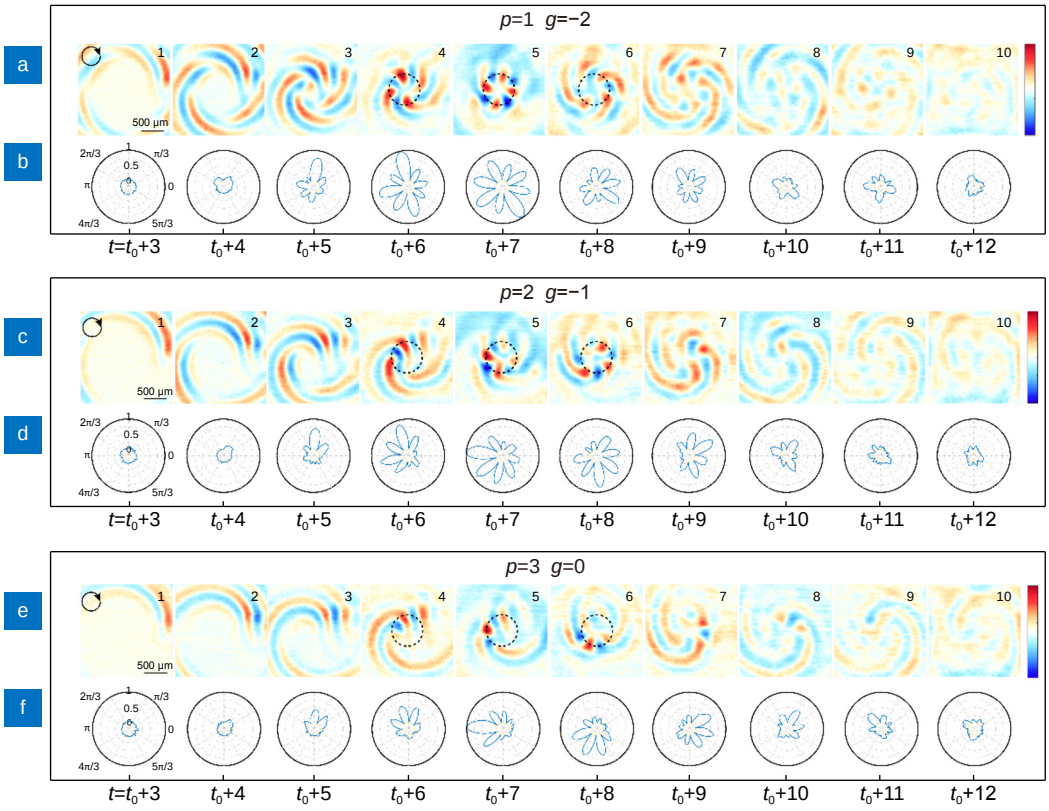

Fig. S7 | Experimental results of the spatiotemporal evolution progress of the generated plasmonic vortices, correspond to the result of samples introducing different propagation phases with δ*R* = *pλ*$_{SP}$, and *p* = 1, 2, 3, respectively. (**a**), (**c**) and (**e**) are the time-resolved snapshots of the SP filed distribution in the *xy*-plane, with an interval of 1 ps. (**b**), (**d**) and (**f**) are the absolute amplitude value of SPs on the target orbit.

Section 7: Tailoring the spatiotemporal dynamics of plasmonic vortex through changing the resonance response of slit resonator.

Since the resonance response of slit resonator directly determines the waveform of the excited SPs, it can also be employed to tailor the spatiotemporal dynamics of plasmonic vortex. Here, we take two different waveforms, shown in Fig. S8(a) and S8(b) for example, corresponding to a lower and higher *Q* resonance than that in the manuscript. The coupler designs are identical with that in Sample 1 ($g = -3$, $p = 0$) and Sample 2 ($g = 1$, $p = 4$), which can also form the fourth-order plasmonic vortex. We carried out numerical investigation including the snapshots of SP filed evolution and the ex-

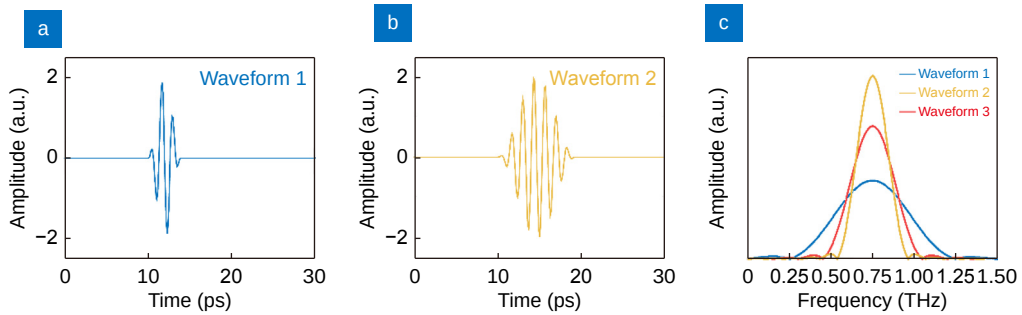

Fig. S8 | (**a**) The excitation waveform 1 of slit resonator resonance which possesses less oscillations than the waveform in the manuscript. (**b**) Waveform 2 of another slit resonator resonance, which possesses more oscillations than that in the manuscript. (**c**) Fourier transformation results of the time-domain signals, waveform 1 in blue, waveform 2 in yellow and the waveform 3 used in the manuscript in red. It can be concluded that waveform 1 and waveform 2 correspond to a lower and higher *Q* resonance than that in the manuscript, with $Q_1 = 0.861$, $Q_2 = 4.673$ and $Q_3 = 2.420$. The *Q* resonance here is defined as the maximum amplitude (normalized by that of waveform 2) divided by the full width at half-maximum.

tracted absolute SP amplitudes on the target orbit. Results are shown in Figs. S9 and S10 for Sample 1 and Sample 2, respectively.

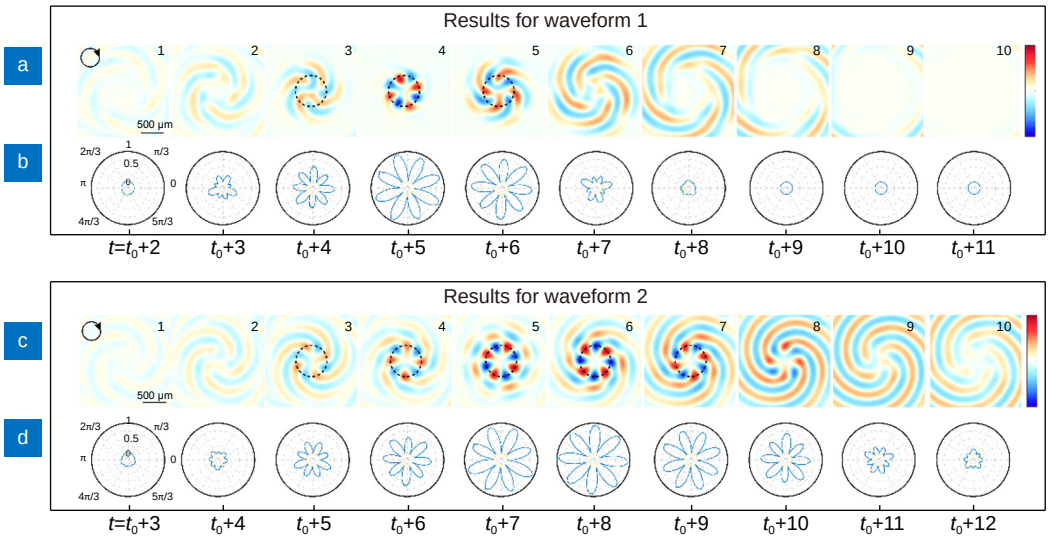

Fig. S9 | The spatiotemporal evolution results of Sample 1 under above two excitation waveforms. (**a**) and (**c**) are snapshots of SP filed in the *xy*-plane with an interval of 1 ps, for waveform 1 and waveform 2. (**b**) and (**d**) are the extracted absolute SP amplitudes on the target orbit labeled by the black dotted circles.

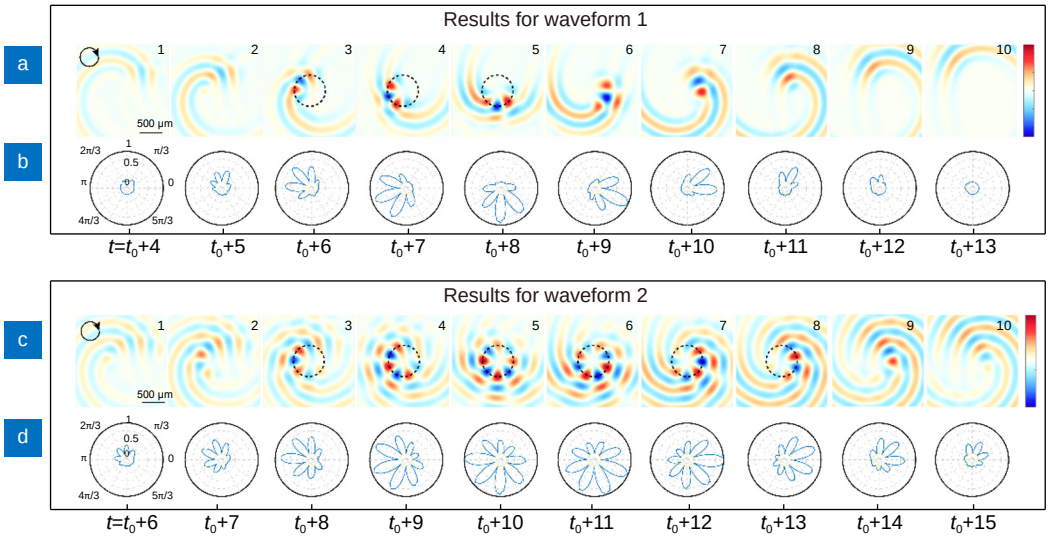

Fig. S10 | The spatiotemporal evolution results of Sample 2 under above two resonance responses of slit resonator. (**a**) and (**c**) are snapshots of SP filed in the *xy*-plane with an interval of 1 ps, for waveform 1 and waveform 2. (**b**) and (**d**) are the extracted absolute SP amplitudes on the target orbit labeled by the black dotted circles.